A Very Metal-poor RR Lyrae Star with a Disk Orbit Found in the Solar Neighborhood

Noriyuki Matsunaga,[1,2] Akinori Itane,[1] Kohei Hattori,[3,4] Juliana Crestani,[5,6] Vittorio Braga,[6,7] Giuseppe Bono,[5,6] Daisuke Taniguchi,[1] Junichi Baba,[3] Hiroyuki Maehara,[3] Nobuharu Ukita,[3] Tsuyoshi Sakamoto,[8] Naoto Kobayashi,[9,10,2] Tsutomu Aoki,[10] Takao Soyano,[10] Ken'ichi Tarusawa,[10] Yuki Sarugaku,[2] Hiroyuki Mito,[11] Shigeyuki Sako,[9] Mamoru Doi,[9] Yoshikazu Nakada,[9] Natsuko Izumi,[12] Yoshifusa Ita,[13] Hiroki Onozato,[3] Mingjie Jian,[1] Sohei Kondo,[10] Satoshi Hamano,[3] Chikako Yasui,[14] Takuji Tsujimoto,[3] Shogo Otsubo,[2] Yuji Ikeda,[15,2] and Hideyo Kawakita[2,16]

[1]Department of Astronomy, School of Science, The University of Tokyo, 7-3-1 Hongo, Bunkyo-ku, Tokyo 113-0033, Japan
[2]Laboratory of Infrared High-resolution spectroscopy (LiH), Koyama Astronomical Observatory, Kyoto Sangyo University, Motoyama, Kamigamo, Kita-ku, Kyoto, 603-8555, Japan
[3]National Astronomical Observatory of Japan, 2-21-1 Osawa, Mitaka, Tokyo 181-8588, Japan
[4]Institute of Statistical Mathematics, 10-3 Midoricho, Tachikawa, Tokyo 190-0014, Japan
[5]Dipartimento di Fisica, Universita di Roma Tor Vergata, via della Ricerca Scientifica 1, I-00133 Roma, Italy
[6]INAF, Osservatorio Astronomico di Roma, via Frascati 33, I-00078 Monte Porzio Catone, Italy
[7]Space Science Data Center, ASI, via del Politecnico snc, I-00133 Roma, Italy
[8]Smile Collection Inc., 4-13-10 Kotobuki, Taito-ku, Tokyo 111-0042, Japan
[9]Institute of Astronomy, School of Science, The University of Tokyo, 2-21-1 Osawa, Mitaka, Tokyo 181-0015, Japan
[10]Kiso Observatory, Institute of Astronomy, School of Science, The University of Tokyo, 10762-30 Mitake, Kiso-machi, Kiso-gun, Nagano 397-0101, Japan
[11]UTokyo Organization for Planetary and Space Science, the University of Tokyo, 7-3-1, Hongo, Tokyo 113-0033, Japan
[12]Institute of Astronomy and Astrophysics, Academia Sinica, No. 1, Section 4, Roosevelt Road, Taipei 10617, Taiwan
[13]Astronomical Institute, Graduate School of Science, Tohoku University, 6-3 Aramaki Aoba, Aoba-ku, Sendai, Miyagi 980-8578, Japan
[14]National Astronomical Observatory of Japan, California Office, 100 W. Walnut St., Suite 300, Pasadena, CA 91124, USA
[15]Photocoding, 460-102 Iwakura-Nakamachi, Sakyo-ku, Kyoto 606-0025, Japan
[16]Department of Astrophysics and Atmospheric Sciences, Faculty of Science, Kyoto Sangyo University, Motoyama, Kamigamo, Kita-ku, Kyoto 603-8555, Japan

ABSTRACT

Metal-deficient stars are important tracers for understanding the early formation of the Galaxy. Recent large-scale surveys with both photometric and spectroscopic data have reported an increasing number of metal-deficient stars whose kinematic features are consistent with those of the disk stellar populations. We report the discovery of an RR Lyrae variable (hereafter RRL) that is located within the thick disk and has an orbit consistent with the thick-disk kinematics. Our target RRL (HD 331986) is located at around 1 kpc from the Sun and, with $V \simeq 11.3$, is among the $\sim$130 brightest RRLs known so far. However, this object was scarcely studied because it is in the midplane of the Galaxy, the Galactic latitude around -1 deg. Its near-infrared spectrum (0.91–1.32 μm) shows no absorption line except hydrogen lines of the Paschen series, suggesting [Fe/H] $\lesssim -2.5$. It is the most metal-deficient RRL, at least, among the RRLs whose orbits are consistent with the disk kinematics, although we cannot determine to which of the disk and the halo it belongs. This unique RRL would provide us with essential clues for studying the early formation of stars in the inner Galaxy with further investigations, including high-resolution optical spectroscopy.

Corresponding author: Noriyuki Matsunaga
matsunaga@astron.s.u-tokyo.ac.jp

1. INTRODUCTION

It is possible to investigate stellar populations in the Galaxy with various detailed observations thanks to relatively low distances to individual stars. For example, the positions and motions of billions of stars provided by the *Gaia* satellite (see Gaia Collaboration et al. 2021, for the latest data release, EDR3) have revolutionized our understanding of the Galactic structure and evolution. In particular, streams and substructures that are clearly detected with the *Gaia* data allow us to build up a scenario of accretions and mergers in the early history of the Galaxy (Helmi 2020). Another vital material for characterizing the Galactic stellar populations is being brought by detailed elemental abundances based on high-resolution spectroscopy (Jofré et al. 2019; Matteucci 2021, and references therein). Metal-deficient stars are especially important for studying the early Galactic evolution (Frebel & Norris 2015), and tremendous efforts have been devoted to identifying metal-deficient stars (see, e.g., Starkenburg et al. 2017; Da Costa et al. 2019, for recent large-scale surveys). An exciting discovery through these surveys is the presence of metal-deficient stars in the Galactic disk (Sestito et al. 2020).

The presence and the characteristics of metal-deficient stars in the disk provide us with crucial clues to the formation of the Galactic disk and its history. A strong merger at an early stage, for example, would have disrupted the disk, and metal-deficient stars that were present at the time of the merger could lose their disk-like kinematics except those in the inner Galaxy where the gravitational potential was deep enough to trap the stars. Recent studies equipped with the *Gaia* data suggest that such a merger occurred ∼10 Gyr ago, triggered the growth of the thick disk (Gallart et al. 2019; Helmi et al. 2018; Helmi 2020), and is imprinted in the kinematics of halo stars as a feature called *Gaia Enceladus* or *Gaia Sausage*. The metal-deficient stars with disk-like orbits such as the stars with [Fe/H] ≤ -2.5 discussed in Sestito et al. (2020) can be considered relics of the proto-disk that was present before the merger. Further identification of such stars over a wide range of metallicity, together with the characterization of halo stars in the same spatial volume, is crucial to establish (or reject) such a formation scenario of the thick disk.

This study focuses on RR Lyrae stars (RRLs) to investigate the old and metal-deficient populations located in the Galactic disk. RRLs are pulsating stars in the Cepheid instability strip and at the horizontal branch phase evolved from low-mass stars ($\lesssim 1\,M_\odot$). They are exclusively old (> 10 Gyr) and thus trace old stellar populations in galaxies. General views on the characteristics of RRLs are found in a review by Beaton et al. (2018) and references therein. The majority of RRLs belong to old stellar spheroids, i.e., the halo and the bulge, while the disk population of RRLs has been also found (Layden 1995; Prudil et al. 2020; Zinn et al. 2020). Other than the differences in spatial distribution and kinematics, an essential difference between the halo and disk groups of RRLs is the metallicity distribution. Disk RRLs are predominantly metal-rich, [Fe/H] $\gtrsim -1$, while halo RRLs are less metal enriched. In this study, we report the discovery of an RRL with [Fe/H] $\lesssim -2.5$ that has a disk-like orbit.

The rest of this paper is organized as follows. First, we discuss the photometric properties of our target in Section 2. We first identified this object as a bright but unexplored RRL through our variability survey, KWFC Intensive Survey of the Galactic Plane (KISOGP), described in Section 2.1. Combined with other photometric data (Section 2.2) and the *Gaia*-based distance, we give an estimate of its metallicity by making use of the period–luminosity–metallicity relation of RRLs (Section 2.3). Then, in Section 3, we present the analysis of the near-infrared spectrum obtained with the WINERED spectrograph. We detected hydrogen lines of the Paschen series, which enable us to measure the radial velocity (Section 3.2), but detected no metallicity lines, which gives only upper limits of abundance (Section 3.3). In Section 4, we discuss the kinematics and the low metallicity of the target RRL in the context of the Galactic structure and evolution. Finally, Section 5 concludes the paper.

2. PHOTOMETRIC DATA

2.1. *KISOGP*

KISOGP is the large-scale survey of variable stars in the northern Galactic plane using Kiso Wide Field Camera (KWFC) attached to the 105-cm Schmidt telescope at Kiso Observatory, Japan. KWFC is a mosaic CCD camera with eight CCD chips having a total of $8\,\mathrm{k} \times 8\,\mathrm{k}$ pixels covering a field-of-view of 2.2 degrees square ($0.946''\,\mathrm{pix}^{-1}$) on the sky. See more details of the KWFC in Sako et al. (2012).

To discover and characterize variable stars in the Galactic plane, we started the KISOGP in 2012
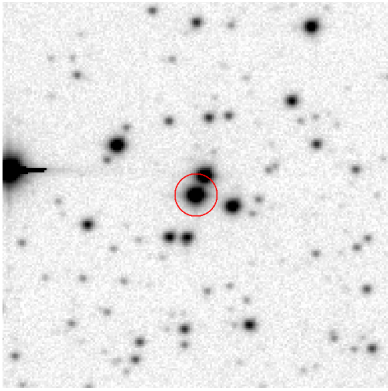
Figure 1. Finding chart of our target RRL (HD 331986), indicated by the red circle with the radius of $10''$, on a KISOGP I-band image (3 arc-minute square, north up and east left).

Table 1. Properties of the target RR Lyr star

Item(s)	Value(s)	Ref.
KISOGP ID	KISOJ 201241.60+321242.4	1
Aliases	HD 331986, NSVS 8487853	2
Gaia EDR3 Source ID	2054159819759156992	3
Eq. coordinate (deg)	$\alpha = 303.17334$, $\delta = 32.21177$	2
Gal. coordinate (deg)	$l = 70.40915$, $b = -1.05159$	2
Valiability type	RRc	1, 2
Period (days)	0.371197	1
2MASS magnitudes	$J = 9.954$, $H = 9.663$	4
	$K_\mathrm{s} = 9.577$	
Astrometric distance (kpc)	1.042 ± 0.015	5
Proper mosion (mas yr^{-1})	$\mu_\alpha \cos \delta = 11.76$, $\mu_\delta = -5.09$	3
	$\mu_l \cos b = 2.23$, $\mu_b = -12.62$	3

References—(1) This work, (2) Simbad, (3) *Gaia* EDR3, (4) Skrutskie et al. (2006), (5) Bailer-Jones et al. (2021)

and made I_c-band time-series observations for the 80 KWFC fields-of-view covering $\sim$330 deg^2 between 60 and 210 deg in Galactic longitude (Matsunaga 2017). The analysis for publishing the catalog of variables detected in the KISOGP is in progress, but a study on eclipsing binary systems has been published by Ren et al. (2021).

During our early attempt to identify periodic variables, we discovered a bright but scarcely-investigated RRL and made a spectroscopic observation in 2015 (Section 3.1). The properties of this RRL variable, HD 331986 (finding chart presented in Figure 1), are summarized in Table 1. The KISOGP I-band light curve of this object is presented in Figure 2 together with light curves in other wavelengths (see Section 2.2).

We fitted the discrete Fourier series to the photometric points,

$$m(t) = A_0 + \sum_{j=1}^{3} A_j \sin \left[\frac{2\pi j}{P}(t - t_0) + \phi_j \right] \quad (1)$$

where t indicates the heliocentric Julian date (HJD) of each photometric measurement and t_0 is the reference epoch, 2456000.519, which we determined to put the maximum of the I_c-band light curve at phase zero. We obtained the period, $P = 0.371197$ days, that gives the maximum power in the periodogram constructed with the three-term Fourier model as given in Equation 1 for the KISOGP light curve (see the methodology, e.g., in VanderPlas 2018). Using the fitted light curve, we calculated the intensity mean and the peak-to-valley amplitude (Table 2). We confirm that this star is a first-overtone mode RRL (RRc type) based on its period, amplitude, and light curve shape.

Figure 2. Light curves of our target RRL (HD 331986). The upper panel presents optical data, i.e., KISOGP (I_c) and *Gaia* DR2 (RP, G, and BP), while the lower panel presents the infrared data from *NEOWISE* (W_1 and W_2). The dashed curves indicate the fitted discrete Fourier series (Equation 1). The gray strip indicates the duration of the WINERED spectroscopic observation (Section 3.1).

Table 2. Mean magnitudes and peak-to-valley amplitudes

Band	I_c	RP	G	BP	W_1	W_2
Mean	10.556	10.648	11.165	11.525	9.519	9.529
Amp	0.365	0.430	0.556	0.661	0.109	0.109

2.2. Other photometric data sets

Our target star was first identified as a candidate of RRL by Kinemuchi et al. (2006) based on the Northern Sky Variability Survey (NSVS). Hoffman et al. (2009) also reported this star as an RRL based on the automated classification with the NSVS data. It has also been included as an RRL in the *Gaia* Data Release 2 (Clementini et al. 2019) and the variability catalog based on the *Wide-field Infrared Survey Explorer* (*WISE*) (Chen et al. 2018). However, no detailed follow-up study has been done, and its kinematic and chemical features remained to be revealed.

As seen in Figure 1, there is a similarly bright star at ∼10″, *Gaia* EDR3 ID 2054159819759157504 with $G = 11.56$. This star is at 0.35 kpc (Bailer-Jones et al. 2021) and has a higher proper motion ∼20 mas yr^{-1}. It does not affect the KISOGP photometry of the target RRL, but severe contamination occurs in the NSVS images with the pixel size of 14.″4 (Kinemuchi et al. 2006). The same applies to the data from the All-Sky Automated Survey for Supernovae (ASAS-SN) with 8.″0 pixels (Jayasinghe et al. 2018). There is no optical data set, other than the *Gaia* DR2, that was published before and gives a high-quality light curve of this object in V or other bands.

We consider the data of 2MASS (Skrutskie et al. 2006) and *NEOWISE* (Mainzer et al. 2011, 2014) for the infrared range. While the 2MASS gives the JHK_s magnitudes at a single epoch (1999 June 22), *NEOWISE* gives time-series data collected between 2014 May and 2020 October in the two mid-IR bands, W_1 (3.4 μm) and W_2 (4.6 μm). The available time-series data are presented in Figure 2, but the 2MASS magnitudes are not included because we cannot determine the precise pulsation phase for this data set ∼30 years ago. We fitted the three-term Fourier series (Equation 1) to the photometric points in each band and estimated the intensity mean and amplitude (Table 2). The *NEOWISE* data include many outliers, and we made 2-σ clipping for fitting the Fourier series. Although we did not find good V-band photometry free from the blending effect as mentioned above, the mean magnitudes in the *Gaia* bands give the mean V-band mean magnitude of 11.32

and the maximum magnitude of 11.01 according to the formula in Evans et al. (2018). Maintz (2005) compiled a catalog of well-identified RRLs brighter than $V = 12.5$ at the maximum phase, and there are 132 RRLs brighter than our target RRL.

2.3. Period–luminosity–metallicity relation

RRLs are established distance indicators although their correlation between period and absolute magnitudes are significantly affected by metallicity (Beaton et al. 2018). We consider the period–luminosity–metallicity (PLZ) relations obtained by Neeley et al. (2019) to see if the photometric data are consistent with the geometric distance and to give a constraint on the metallicity of our target. Following a theoretical study on the PLZ relation in Neeley et al. (2017), Neeley et al. (2019) used the *Gaia* DR2 trigonometric distances of 55 RRLs with [Fe/H] between −2.56 and −0.07 to obtain the empirical PLZ relations from optical to mid-IR photometric bands. The PLZ relation in each band is in the form of

$$M_\lambda = a + b(\log P_F + 0.30) + c([Fe/H] + 1.36), \quad (2)$$

where P_F is the "fundamentalized" period given by $\log P_F = \log P + 0.127$ for an RRc star ($\log P_F = -0.303$ for our target). The mid-IR bands used in Neeley et al. (2019) are those of the *Spitzer* Space Telescope, but we use their PLR relations for the *WISE* data. The *Spitzer* [3.6] and [4.5] bands correspond to the *WISE* W_1 and W_2 bands, respectively. The theoretical result by Neeley et al. (2017) suggests that the relations in the *Spitzer* bands and those in the *WISE* bands identical, within 0.003 mag, with each other at each wavelength. In addition to W_1, W_2, and I_c in Table 2, we consider the single-epoch 2MASS magnitudes in JHK_s in the following analysis.

Combining an observed magnitude (m_λ) and the PLZ relation (Equation 2), we can calculate the distance modulus as a function of [Fe/H],

$$\mu_\lambda = \mu_0 + A_\lambda = m_\lambda - M_\lambda, \quad (3)$$

where μ_λ and μ_0 are called *apparent* and *true* distance moduli, respectively, and A_λ indicates the interstellar extinction at each wavelength. In the upper panel of Figure 3, the *apparent* distance moduli with different [Fe/H] are compared with each other and also with the distance modulus corresponding to the astrometry-based distance in Bailer-Jones et al. (2021). We adopt the extinction law obtained by Wang & Chen (2019), i.e., $A_{I_c}/A_V = 0.559$, $A_J/A_V = 0.243$, $A_H/A_V = 0.131$, $A_{K_s}/A_V = 0.078$, $A_{W_1}/A_V = 0.039$, and $A_{W_2}/A_V = 0.026$.

We can predict a model of μ_λ for a given set of A_V and [Fe/H], like the one indicated by the orange curve in Figure 3, and we searched for the best set with the least-square method. We used the error of 0.10 mag for the 2MASS JHK_s and 0.03 mag for the other bands considering that the 2MASS data are single-epoch magnitudes. We then obtained $A_V = 1.01$ and [Fe/H] $= -2.55$ by searching for the best set of these parameters that makes the six-band photometry in Figure 3 consistent with the *true* distance modulus based on the astrometry-based distance. This result indicates that our target RRL is very metal poor ([Fe/H] < -2, according to the terminology in Beers & Christlieb 2005), which is consistent with the spectroscopic analysis we present in Section 3. The higher [Fe/H] would require the lower distance as illustrated in Figure 3. This estimate is subject to the systematic uncertainty and the intrinsic scatter of the PLZ relations given by Neeley et al. (2019) in addition to the uncertainty in the *Gaia*-based distance by Bailer-Jones et al. (2021). It is not straightforward to estimate the error in our estimate considering various uncertainties discussed in Neeley et al. (2019). We roughly estimate that the distance modulus based on the PLZ has the error of 0.1 mag, which dominates the error $\sim$0.03 mag from the *Gaia*-based distance, and the error of 0.1 mag corresponds to the error of $\sim$0.5 in [Fe/H].

The light curve shape can be used to infer the metallicity of RRab-type variables(see Mullen et al. 2021, and references therein) but not for RRc-type ones. Nevertheless, the period and amplitudes indicate that this RRc star is metal-deficient compared to typical RRLs. Although there is a star-to-star scatter, Fig. 7 of Sneden et al. (2018) clearly suggests that RRc stars with longer period tend to have lower metallicity. Among the sample they considered, the relatively long period, 0.371197 days, of the target RRL was not found among metal-rich RRc stars ([Fe/H] > -1). Furthermore, Fabrizio et al. (2021) illustrated that metal-deficient RRLs tend to have larger amplitudes at a given period (see their Figure 7). Although we have no good V-band light curve, the amplitudes in the *Gaia* bands suggest a large V-band amplitude, 0.55–0.65 mag, which is found among metal-deficient RRLs ([Fe/H] $\lesssim -1.5$).

3. SPECTROSCOPIC DATA

3.1. *The WINERED spectrum*

We observed the target RRL on 2015 August 15, 14:55 to 16:20 (UT) with WINERED attached to the 1.3 m Araki telescope at Koyama Observatory, Kyoto Sangyo University in Japan. WINERED is a near-infrared high-resolution spectrograph covering 0.90 to 1.35 μm (z', Y, and J bands) with the resolution of $R = \lambda/\Delta\lambda = 28000$
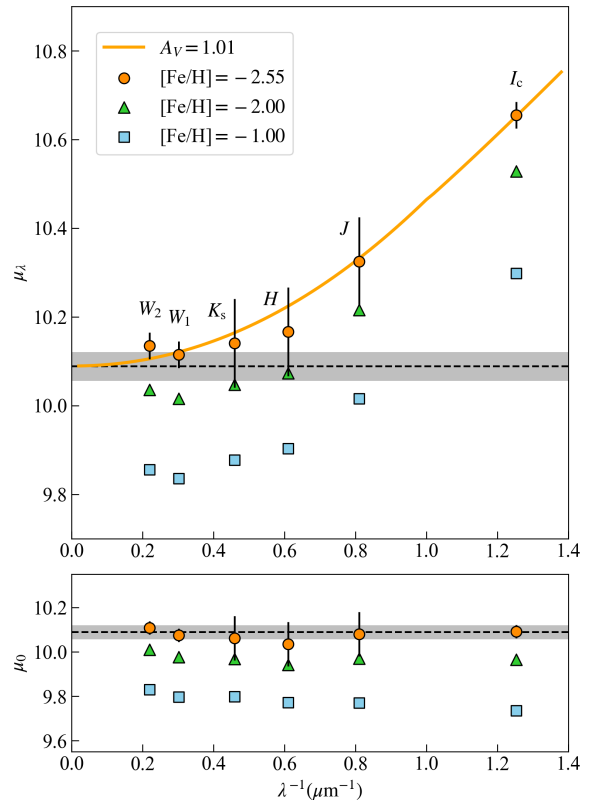
Figure 3. The *apparent* distance moduli μ_λ (upper panel) and the *true* distance moduli μ_0 (lower panel) obtained with different photometric bands. The horizontal gray line and strip indicate the astrometry-based distance modulus and its error obtained by Bailer-Jones et al. (2021). The interstellar extinction corresponding to $A_V = 1.01$ is used to draw the orange curve in the upper panel and to convert μ_λ to μ_0 at each band.

with the WIDE mode (Ikeda et al. 2016, 2021). We carried out eight 600 s exposures, giving the total integration time of 4800 s, with the ABBA nodding pattern having the target within the slit in all the exposures. The eight exposures within $\sim$1.4 hours cover the phases between 0.47 and 0.63 along the pulsation cycle (Figure 2).

The raw spectral data were first reduced by the pipeline developed by the WINERED team (Hamano et al. in preparation). The pipeline outputs one-dimensional spectra for individual exposures and combined spectra along with supplementary information. Avoiding the spectral parts with too much telluric absorption, we consider the following echelle orders in the subsequent analysis: 43th to 48th (11560–13190 Å in the J band), 51st to 57th (9760–11150 Å in the Y band), and 61st (9120–9280 Å in the z' band).

Having the spectra from eight exposures allows us to reject spurious noises before making the combined spec-

tra and to estimate the signal-to-noise ratio (S/N) as follows. We compared the eight one-dimensional spectra after the continuum normalization produced by the pipeline and calculated the mean (μ) and the standard deviation (σ) of the fluxes at each wavelength. We then rejected the signals from individual exposures (f_i) if $|f_i - \mu| > 2\sigma$ and calculated the mean and its standard error using the accepted signals. Thus, we obtained the combined spectrum, which is less affected by outliers, and the realistic estimates of errors in individual pixels. We estimated the S/N of each echelle order by considering the median of the pixel-by-pixel errors in the normalized flux. The S/N in the final spectrum per pixel ranges from 45 to 70 except the 61st order with S/N$\sim$ 30 in which the telluric absorption is rather severe.

We then performed the telluric correction using the synthetic telluric absorption calculated with *Telfit* tool (Gullikson et al. 2014). We actually observed an A0V star, 29 Vul, as a telluric standard star with the total integration time of 600 s (two 300 s exposures). However, hydrogen lines are the main features we study, and using the spectrum of a telluric standard star which shows its own hydrogen lines would disturb the profiles of the hydrogen lines of our target. After the telluric correction, we made the continuum normalization again.

The reduced spectrum is featureless except strong hydrogen lines and spurious noises that are mainly caused by residuals of telluric lines and OH airglow lines (Oliva et al. 2015). We use the hydrogen lines to measure the radial velocity (Section 3.2), and we estimate the upper limits of chemical abundance with the help of theoretical synthetic spectra (Section 3.3).

3.2. *Hydrogen lines*

There are four hydrogen lines situated within the wavelength range of our interest, and we detected all of them (Figure 4). Pa ϵ at 9545.973 is located in the 59th order of our spectrum, but it is too much contaminated by the telluric absorption in between the z' and J bands. We measured the central wavelength (λ_{obs}) and FWHM by fitting a Gaussian function to 20 pixels, corresponding to ± 50 km s^{-1}, around each of the four hydrogen line. Table 3 lists λ_{obs} and the air wavelength at rest, λ_{air}, together with the radial velocity and the FWHM. The velocity error in the fitting of a Gaussian is smaller than 1 km s^{-1}.

In order to calculate the barycentric motion of the object, however, we need to consider the pulsational effect in addition to the heliocentric correction (i.e., the correction taking into account the motion of the observing facility around the Sun). The amplitude of radial velocity (Δ_{RV}) is, at least approximately, proportional to the
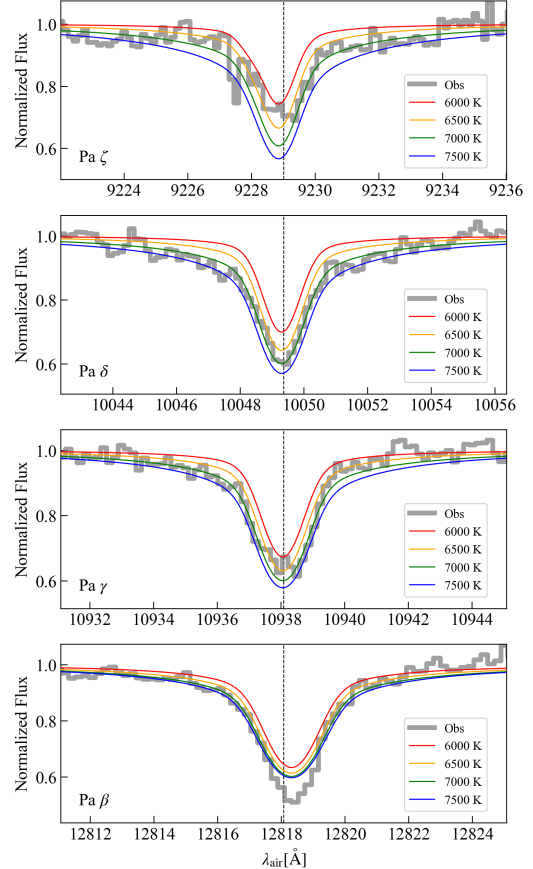
Figure 4. Four hydrogen lines, from Pa ζ (top) to Pa β (bottom), located within the WINERED spectrum. Vertical line corresponds to the air wavelength, λ_{obs}, of each line at rest. The wavelength scale of the observed spectrum (Obs) is after the mean radial velocity, -85.5 km s^{-1}, subtracted. Four synthetic spectra with $\log g = 2.6$ and [Fe/H] $= -2$ but with different T_{eff} are adjusted to the observed spectrum considering the differences between the mean velocity and v_i in Table 3.

Table 3. Four hydrogen lines detected (Paschen series)

Line	λ_{air}	λ_{obs}	v_i	FWHM
	(Å)	(Å)	(km s^{-1})	(km s^{-1})
Pa ζ	9229.017	9226.247	-90.0	78.6
Pa δ	10049.373	10046.462	-86.9	60.8
Pa γ	10938.093	10934.966	-85.8	62.1
Pa β	12818.077	12814.689	-79.3	51.2
Mean			-85.5	

V-band amplitude (Δ_V) (Sneden et al. 2017; Magurno et al. 2019). Recently, Braga et al. (2021) thoroughly investigated the amplitudes and shapes of velocity curves obtained with different absorption lines in the optical range and provided templates of velocity curve. The ratio Δ_{RV}/Δ_V depends on the line being measured. In particular, H$_\alpha$ gives a large ratio, $\Delta_{RV}/\Delta_V \simeq 107$, compared to other Balmer lines and metallic lines, which give the ratios ~ 55 with some scatter for RRc stars. Unfortunately, the ratios for the Paschen lines have not been studied well. Therefore, we make a simple correction by ignoring the difference between the velocity curves of the four Paschen lines and assuming $\Delta_{RV}/\Delta_V = 55$. This ratio is also consistent with the ratios reported by Sneden et al. (2017) and Magurno et al. (2019). The amplitudes in the *Gaia* bands indicate that the V-band semi-amplitude ~ 0.3 mag, leading to the semi-amplitude of velocity ~ 16.5 km s^{-1}. The radial velocity of an RRc star gets most redshifted at around the minimum phase with respect to the mean velocity (e.g., Benkő et al. 2021). Thus, we apply the correction of -16.5 km s^{-1} in addition to the heliocentric correction (-2.4 km s^{-1}), resulting in the heliocentric velocity $V_{\rm helio} = -104.4$ km s^{-1} and the velocity with respect to the local standard of rest (LSR) $V_{\rm LSR} = -86.7$ km s^{-1}. Because of the lack of the velocity template and because only a single-epoch velocity measurement is available, the correction of the pulsational effect introduces the dominant error in our estimate of the barycentric radial velocity (or so-called gamma velocity, V_γ). Considering the scatter of Δ_{RV}/Δ_V observed in different RRc stars and the line-to-line difference presented in Braga et al. (2021, see their Fig 15), we conservatively estimate its error to be 10 km s^{-1}.

3.3. *Metallic lines*

We detected no metallic lines, and we cannot make any solid estimate of the chemical abundance of the target RRL. Instead, we estimate the upper limits of the equivalent widths (EWs) and the corresponding limits of abundance for the strongest absorption lines expected in the WINERED range.

3.3.1. *Spectral synthesis and stellar parameters*

In the subsequent analysis, we used the MOOG tool for spectral synthesis (Sneden et al. 2012) together with the ATLAS9 atmosphere models extended by Mészáros et al. (2012). They provided the models with different [α/Fe] and [C/Fe] for a wide range of metallicity, and we assumed [α/Fe] and [C/Fe] are both enhanced by $+0.3$ dex. Together with an atmospheric model, the spectral synthesis requires a list of absorption lines. We considered Vienna Atomic Line Database (VALD;

Ryabchikova et al. 2015) and the list of Meléndez & Barbuy (1999; hereinafter referred to as MB99), and synthesized two spectra for a given atmospheric model by using the two line lists separately.

We need stellar parameters such as the effective temperature to decide which atmosphere models we use. The WINERED observation was carried out over ~ 1.4 hours, within which 10-min exposures were repeated eight times). This corresponds to a significant fraction of the pulsation cycle, $0.473 < \phi < 0.630$ (Figure 2). Nevertheless, the variation of stellar parameters is expected to be small because the exposures were made at around the minimum phase (e.g., Govea et al. 2014). Therefore, we decided to ignore the variation of stellar parameters during the eight exposures.

It is, however, not easy to obtain a precise estimate of the stellar parameters of our target. In Section 2.3, we used the PLZ relations to estimate the interstellar reddening. This means that we assumed that the intrinsic color of our target is consistent with the prediction of the PLZ relations for which only mean magnitudes are used. On the other hand, the lack of metallic lines prevents us from estimating the stellar parameters with various methods used in common spectral analyses. Therefore, we consider the $T_{\rm eff}$ and $\log g$ expected for RRc-type variables allowing relatively large errors.

Govea et al. (2014) found that $T_{\rm eff}$ of RRc are concentrated in between 7000–7500 K. This is consistent with $T_{\rm eff}$ of a larger sample of RRc stars in Crestani et al. (2021b) considering the uncertainties. At around the minimum phase, the effective temperature is expected be at the low extreme. We consider three temperatures, i.e., 6750, 7000, and 7250 K, where we need to evaluate the effect of $T_{\rm eff}$ on the upper limits of abundance. Concerning other stellar parameters necessary for the spectral synthesis, we use the surface gravity $\log g = 2.6$, the microturbulence $v_{\rm mic} = 2.5$ km s^{-1}, and the additional Gaussian broadening $v_{\rm broad} = 25.0$ km s^{-1} including the macroturbulence and instrumental factors. Figure 4 compares the observed spectrum with synthetic spectra with $\log g = 2.6$ and [Fe/H] $= -2$ but with four different $T_{\rm eff}$ between 6000 and 7500 K. The relative strengths of the four Paschen lines support the adopted temperature range. The constraint is, however, not very strong because it is hard to reproduce the broad profile of hydrogen lines accurately with high-resolution echelle spectra like the WINERED one.

3.3.2. *Upper limits of equivalent width*

We first listed up the supposedly strongest absorption features in the synthetic spectrum with $T_{\rm eff} = 7000$ K, $\log g = 2.6$, and [Fe/H] $= -1$ created with the line list of VALD or MB99. Then, we identified the absorption

Table 4. Upper limits of equivalent width (W) and [X/H] for the metallic lines selected from VALD

ID	Species	λ_{air} (Å)	EP (eV)	$\log gf$	W_{up} (mÅ)	[X/H]$_{\mathrm{up}}$
V01	S I	9212.8630	6.524	0.470	52	−1.72
V02	Mg II	9218.2500	8.655	0.270	85	−1.08
V03	Si I	10585.141	4.954	0.012	28	−1.99
V04	C I	10683.080	7.483	0.079	86	−2.10
V05	C I	10685.340	7.480	−0.272	103	−1.57
V06	C I	10691.245	7.488	0.344	72	−2.51
V07	C I	10707.320	7.483	−0.411	48	−2.05
V08	C I	10729.529	7.488	−0.420	38	−2.18
V09	Si I	10827.088	4.954	0.302	44	−2.03
V10	Si I	10868.789	6.191	0.206	39	−2.11
	Si I	10869.536	5.082	0.371		
V11	Mg II	10914.244	8.864	0.020	39	—[a]
	Sr II	10914.887	1.805	−0.638		
V12	C I	11658.820	8.771	−0.278	144	−1.03
	C I	11659.680	8.647	0.028		
V13	C I	11748.220	8.640	0.375	61	−1.78
V14	C I	11753.320	8.647	0.691	46	−2.35
V15	C I	11754.760	8.643	0.542	42	−2.32
V16	Mg I	11828.171	4.346	−0.333	57	−1.89
V17	Ca II	11838.997	6.468	0.312	90	−1.66
V18	Si I	11984.198	4.930	0.239	70	−1.69
V19	Si I	12031.504	4.954	0.477	351	—[b]
V20	Mg I	12083.278	5.753	0.450	52	−2.03
	Mg I	12083.649	5.753	0.410		

[a] No constraint was obtained for this feature with multiple elements' contribution.

[b] No constraint stronger than [X/H]≤ -1 was given.

Table 5. Same as Table 4 but for MB99

ID	Species	λ_{air} (Å)	EP (eV)	$\log gf$	W_{up} (mÅ)	[X/H]$_{\mathrm{up}}$
M01	C I	10123.87	8.54	−0.09	51	−1.44
M02	Si I	10585.14	4.95	−0.06	28	−1.92
M03	C I	10683.09	7.48	0.03	86	−2.05
M04	C I	10685.36	7.48	−0.30	103	−1.54
M05	C I	10691.26	7.49	0.28	72	−2.45
M06	C I	10707.34	7.48	−0.41	48	−2.05
M07	C I	10729.54	7.49	−0.46	38	−2.14
M08	Si I	10749.39	4.93	−0.21	46	−1.49
M09	Si I	10827.10	4.95	0.23	44	−1.95
M10	Si I	10869.54	5.08	0.36	39	−2.09
M11	Mg II	10914.24	8.86	0.00	39	—[a]
	Sr II	10914.88	1.80	−0.59		
M12	C I	11658.85	8.77	−0.36	144	—[b]
	C I	11659.70	8.65	−0.07		
M13	C I	11748.24	8.64	0.40	61	−1.81
M14	C I	11753.32	8.65	0.69	46	−2.33
M15	C I	11754.79	8.64	0.51	42	−2.29
M16	Mg I	11828.19	4.35	−0.50	57	−1.72
M17	Ca II	11838.99	6.47	0.24	90	−1.59
M18	Ca II	11949.76	6.47	−0.04	43	−1.92
M19	Si I	11984.23	4.93	0.12	70	−1.57
M20	Si I	12031.53	4.95	0.24	351	—[b]

[a] No constraint was obtained for this feature with multiple elements' contribution.

[b] No constraint stronger than [X/H]≤ -1 was given.

lines that form the selected features (Tables 4 and 5). Multiple lines can contribute to each feature. Among the selected features, the one at 11659.5 Å is formed by two C I lines, and the one at 12083.5 Å by two Mg I lines according to VALD. In addition, Mg II 10914.244 and Sr II 10914.887 could have formed the feature at ~10914.5 Å together. We excluded this mixed feature from the subsequent analysis to avoid the blending effect on the upper limits of abundance.

For each selected feature, we evaluated the upper limits of the EW as follows. First, we calculated the weighted mean and its error of the pixel counts within $\pm 150\,\mathrm{km\,s^{-1}}$ around each line but with the pixels within $\pm 25\,\mathrm{km\,s^{-1}}$ of the features in Tables 4 and 5 excluded from the calculation. The weighted mean is considered as the local continuum level, f_{c} (with the error, e_{c}), in the wavelength range around the feature. If the continuum normalization for each order were

perfect in the spectral reduction (Section 3.1), f_{c} should be 1, and it is actually consistent with 1 within the error in most cases. Then, we obtained the EW (W) and its error (E_W) by

$$W = \sum_{i=1}^{n} \left(1 - \frac{f_i}{f_{\mathrm{c}}} \right) \Delta\lambda_i \tag{4}$$

$$E_W = \frac{1}{f_{\mathrm{c}}} \sqrt{ \sum_{i=1}^{n} \sigma_i^2 (\Delta\lambda_i)^2 + \frac{e_c}{f_{\mathrm{c}}^2} \sum_{i=1}^{n} f_i \Delta\lambda_i } \tag{5}$$

where the sum was taken over the n pixels ($1 \leq i \leq n$, with the flux f_i and the noise σ_i at each pixel) within $\pm 25\,\mathrm{km\,s^{-1}}$ around the line center and $\Delta\lambda_i$ indicates the width of each pixel in the unit of mÅ. We estimated the upper limit of EW by

$$W_{\mathrm{up}} = \begin{cases} W + 3\,E_W & (\text{if } W \geq 0) \\ 3\,E_W & (\text{if } W < 0) \end{cases} \tag{6}$$

for each feature (Tables 4 and 5).
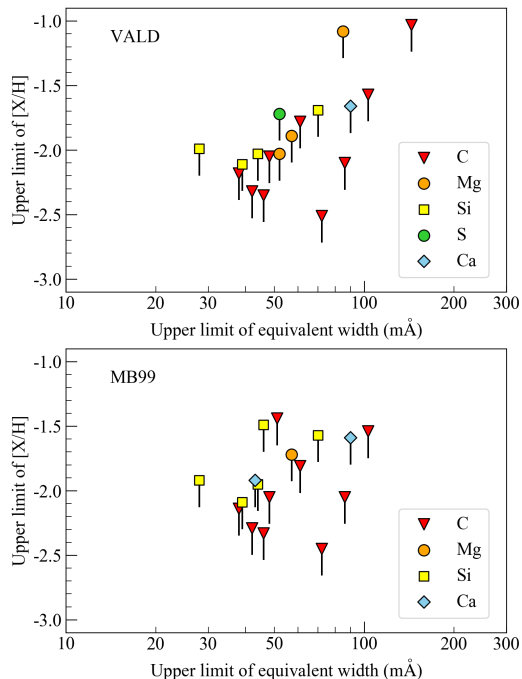
Figure 5. Upper limits of [X/H] given by individual lines in Table 4 (VALD) and those in Table 5 (MB99).

3.3.3. *Upper limits of elemental abundance*

We estimated the upper limits of chemical abundance based on the upper limits of EW. This was done with the help of synthetic spectra. For each feature in Tables 4 and 5, except the mixed feature of Mg II and Sr II at 10914.6 Å, we calculated the EWs in the synthetic spectra with different abundances of each species over $-3 \leq$ [Fe/H] ≤ -1. This enables us to draw the curve of growth and estimate the upper limit which corresponds to $W_{\rm up}$. We estimated the abundance upper limits with the models at three different temperatures (6750, 7000, and 7250 K), and took the highest upper limit of the three as the final estimate, $[{\rm X/H}]_{\rm up}$ in Tables 4 and 5, based on the given feature. The maximum metallicity of the synthetic spectra we considered is -1 dex. If $W_{\rm up}$ is larger than the maximum EW that we found with the synthetic spectra, we give no constraint on the abundance for a given line.

Figure 5 plots the upper limits of abundance. For most of the lines included in both VALD (Table 4) and MB99 (Table 5), the $\log gf$ in the two lists agree with each other within 0.1 dex, and the difference in the line list is not important for the upper limits in Figure 5. Neutral carbon lines give the strongest constraints in terms of [X/H], i.e., [C/H]$\lesssim -2.5$. A couple of lines of other elements (Mg, Si, and Ca) indicate [X/H] $\lesssim -2$. We have no direct constraint on [Fe/H] because no iron line in the WINERED wavelength range is expected to be so strong as the lines in Tables 4 and 5. There have been several reports of carbon-enhanced stars among metal-deficient RRLs (e.g., Preston et al. 2006; Kinman et al. 2012; Kennedy et al. 2014). In contrast, Andrievsky et al. (2020) found [C/Fe]< 0 for a few RRLs with $-1.7 \leq$ [Fe/H] ≤ -1.2

based on the non-local-thermodynamic-equilibrium (NLTE) analysis. We simply give the upper limit of -2.5 dex. and use it in the subsequent discussion. According to the terminology defined by Beers & Christlieb (2005), the target RRL is a very metal-poor star ([Fe/H] < -2) if it is not an extremely metal-poor star ([Fe/H] < -3).

4. DISCUSSION

Combining the radial velocity estimated with the four Paschen lines (Section 3.2) with the *Gaia*'s distance and proper motions, the six-dimensional information (i.e., the position and space velocity) is available for our target. We computed the target's orbital and kinematic properties by taking into account the observational uncertainties. We used the AGAMA package (Vasiliev 2019) with the Galactic constants adopted from Zinn et al. (2020): the distance to the Galactic center $R_0 = 8.2$ kpc, the velocity of the local standard of rest (LSR) $v_{\rm LSR} = 232$ km s^{-1}, and the solar velocity with respect to the LSR being $(U_\odot, V_\odot, W_\odot) = (-11.1, 12.24, 7.25)$ km s^{-1} (Schönrich et al. 2010). We used the Galactic potential called MWPotential2014 available in the galpy library (Bovy 2015), which is composed of three axisymmetric potentials for the spherical power-law bulge with an exponential cut-off, a Navarro-Frenk-White halo potential, and a Miyamoto-Nagai disk.

We randomly drew 10000 samples from the error distribution of the position and velocity and integrated the orbit forward in time for a long enough period of time (100 Gyr). The average and standard deviation of the orbital parameters from individual Monte-Carlo samples are given in Table 6. The eccentricity is defined by $e = (r_{\rm max} - r_{\rm min})/(r_{\rm max} + r_{\rm min})$. The positive azimuthal velocity (v_θ) and angular momentum (L_Z) correspond to the prograde rotation. With the maximum height $z_{\rm max} = 1.18$ kpc from the Galactic plane, the orbit of the target RRL is accommodated within the stretch of the thick disk whose vertical scale length is about 0.9 kpc (Bland-Hawthorn & Gerhard 2016).

In Figures 6 and 7, we compare the properties of our target RRL with 463 RRLs compiled by Zinn et al. (2020), but we re-calculated their parameters except [Fe/H] and V-band magnitudes. We combined the radial velocities adopted from Zinn et al. (2020) with the astrometric data from the *Gaia* EDR3 and the EDR3-based distances from Bailer-Jones et al. (2021) to calculate the current positions (X, Y, and Z), the velocities (v_R, v_θ, and v_Z), the apocenter distance ($r_{\rm max}$), the maximum height ($z_{\rm max}$), the angular momenta (L_Z), and the total orbital energies ($E_{\rm tot}$, the sum of kinetic and potential energies). The total orbital energies show a systematic offset, $\sim 7 \times 10^4$ km^2 s^{-2}, between our calculation and that of Zinn et al. (2020) because of the difference in the Galactic potential. The distributions in the other parameters do not show such systematic offsets but the parameters of individual objects are expected to be improved by using the *Gaia* EDR3.

Figure 6 includes 360 RRLs with $V < 13$, while our RRL is located at $V = 11.32$, obtained in Section 2.2 using the *Gaia* photometry. We highlight eight bright and metal-deficient ([Fe/H] $\lesssim -2.3$) objects selected within Figure 6 and list their names in the caption. Three of them (V338 Pup, X Ari,

Table 6. Kinematic properties of the target RR Lyr star

Parameter	Value
Input parameters	
D_0—geometric distance	1.042 ± 0.015 (kpc)
$v_{\rm helio}$—radial velocity	-104 ± 10 (km s^{-1})
$\mu_\alpha \cos\delta$—proper motion along α	11.76 ± 0.01 (mas yr^{-1})
μ_δ—proper motion along δ	-5.09 ± 0.02 (mas yr^{-1})
Output parameters	
$r_{\rm min}$—pericenter distance	3.71 ± 0.38 (kpc)
$r_{\rm max}$—apocenter distance	8.36 ± 0.01 (kpc)
$z_{\rm max}$—maximum height	1.18 ± 0.01 (kpc)
e—eccentricity	0.39 ± 0.04
$v_{\rm R}$—radial velocity	52.9 ± 2.2 (km s^{-1})
v_θ—azimuthal velocity	143.5 ± 9.8 (km s^{-1})
v_Z—vertical velocity	-53.6 ± 0.3 (km s^{-1})
$v_{\rm pec}$—peculiar velocity	118.7 ± 8.4 (km s^{-1})
$E_{\rm tot}$—total orbital energy	-118.9 ± 1.3 (10^3 km^2 s^{-2})
L_Z—azimuthal angular momentum	1135 ± 77 (kpc km s^{-1})

Note—The given errors are the standard deviation observed in our Monte-Carlo calculation and do not include the systematic errors. The velocity and proper motion of the *input parameters* are given with respect to the Sun, while the velocities of the *output parameters* are given with respect to the Galactic center.
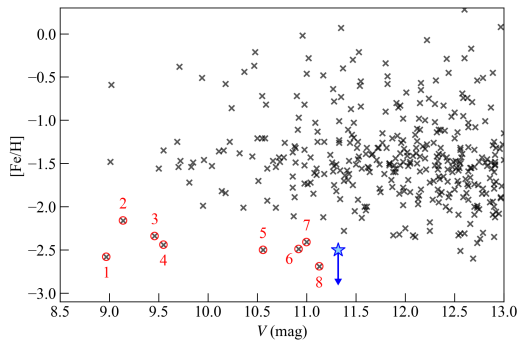
Figure 6. The metallicities and V-band magnitudes of the target RRL (blue) and the known RRLs compiled by Zinn et al. (2020). The metallicity upper limit of the target RRL is indicated by the star symbol accompanied by arrow. Red circles highlight the bright and metal-deficient objects we selected for comparisons (see text): 1=MT Tel, 2=V338 Pup, 3=RZ Cep, 4=X Ari, 5=V701 Pup, 6=UY Boo, 7=TV Boo, and 8=ASAS 200431−5352.3.

and UY Boo) are fundamental-mode pulsators (i.e., RRab type), while the other five are first-overtone pulsators (RRc, same as the target RRL). The metallicities of the eight RRLs have been measured and reported recently in Beers et al. (2014), Sneden et al. (2017), Andrievsky et al. (2018), Cha-

did et al. (2017), and Zinn et al. (2020). The brighter four RRLs (No. 1–4) are located at 0.4–0.6 kpc from the Sun, while the fainter four are further, at 0.95–1.3 kpc, according to Bailer-Jones et al. (2021). The distance to our target RRL is among the more distant ones, and its metallicity is as low as the eight RRLs.

The panel (a) of Figure 7 presents the Toomre diagram, in which the semi-circle contours indicate constant peculiar velocities,

$$v_{\rm pec} = \sqrt{v_R^2 + (v_\theta - v_{\rm LSR})^2 + v_Z^2}, \tag{7}$$

with respect to the LSR corresponding to 75 and 150 km s^{-1}. The panel (b) presents that the RRLs with relatively small $v_{\rm pec}$ tend to be metal-rich (Layden 1995). In Figure 7, except the panel (c), halo stars show more-or-less symmetric distributions of v_θ and L_Z, and they overlap with the disk component at around the position of our target. Bright and metal-deficient RRL highlighted in Figures 6 and 7 can be classified as halo objects according to their $v_{\rm pec}$. The motion of our RRL star deviates significantly from the Galactic rotation with $v_{\rm LSR} = 232$ km s^{-1}, but the star is, with the peculiar velocity of 116.6 km s^{-1}, indistinguishable from thick-disk stars in regards to the kinematics (Figure 7a). Our RRL may still belong to the halo and its motion is at the prograde-side tail of halo orbits. Two metal-deficient bright RRLs highlighted, V338 Pup and V701 Pup (Nos. 2 and 5), are located at around the opposite point on the retrograde side.

The panel (c) plots $z_{\rm max}$ against $r_{\rm max}$ estimated with the orbit calculation. Like our RRL, the orbits of the four bright, metal-deficient RRLs highlighted are within the stretch of the thick disk, although three of them show retrograde motion. In addition, the four RRLs have larger eccentricity than our RRL: 0.53 (V338 Pup), 0.60 (V701 Pup), 0.79 (TV Boo), and 0.83 (X Ari) in contrast to 0.39 of our RRL. Nevertheless, the kinematics of all these very metal-poor RRLs, including our target RRL, is consistent with that of similarly metal-deficient stars investigated by Chiba & Beers (2000), who concluded that the disk population is negligible at [Fe/H] ≤ -2.2. In a recent study on a large sample of stars towards the Galactic anticenter, Fernández-Alvar et al. (2021) detected metal-poor stars belonging to the thin disk well down to [Fe/H] $\simeq -2$ but the situation of more metal-deficient stars was not conclusive.

The panel (d) of Figure 7 plots $E_{\rm tot}$ against L_Z. Zinn et al. (2020) found that, in addition to the RRLs that may be related to moving groups like the Helmi stream (Helmi et al. 1999), there are two major groups, i.e., the 'disk' RRLs with prograde rotation and the 'Plume' RRLs with $L_Z \sim 0$. These two groups of RRLs were also found by Prudil et al. (2020) and Iorio & Belokurov (2021). The Plume structure of halo stars was discovered by Dinescu (2002), and recent studies based on *Gaia* data identified the very prominent feature called *Gaia Enceladus* or *Gaia Sausage* (Belokurov et al. 2018; Helmi et al. 2018). This prominent feature is considered to originate from an accreted galaxy that contributed many halo objects, including globular clusters such as ω Cen after the major merger with the Milky Way (Belokurov et al. 2018; Helmi et al. 2018). Zinn et al. (2020) found that
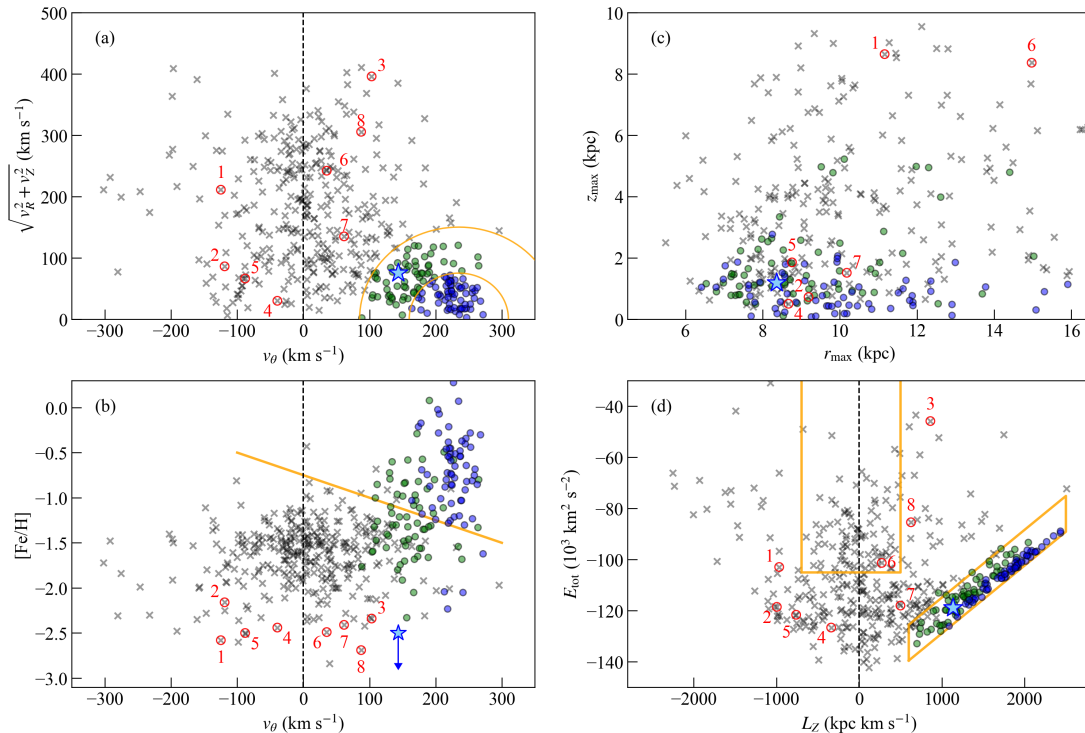
Figure 7. Properties of the target RRL in comparison with the known RRLs compiled by Zinn et al. (2020). The target RRL is indicated by the star symbol, and the arrow in panel (b) means that its metallicity is given as the upper limit. The orange semi-circles in panel (a) indicate the peculiar velocities v_{pec} of 75 and 150 km s^{-1}. The RRLs with v_{pec} smaller than 75 km s^{-1}, are indicated by blue circles, and those with v_{pec} between 75 and 150 km s^{-1} by green circles, and the other RRLs from Zinn et al. (2020) are indicated by gray crosses. The same bright and metal-deficient RRLs as in Figure 6 are indicated by red circles with the number IDs labelled. The orange line in panel (b) indicates the threshold, $v_\theta = -400\,[\mathrm{Fe/H}] - 300$, used for selecting disk RRLs by Layden et al. (1996), while the regions enclosed by orange lines in panel (d) indicate the "Plume" (center) and the "disk" (right).

Plume RRLs include fewer objects with [Fe/H] < -2, and, among the eight highlighted objects, UY Boo (No. 6) is the only one located within the Plume region in Figure 7(d).

Our RRL does not belong to the Plume but is associated with, or at least closer to, the disk populations as discussed above. There are accumulating reports and discussions on the presence of metal-deficient stars in the thick disk (Di Matteo et al. 2020; Sestito et al. 2020; Limberg et al. 2021). The latter two authors used large samples of more than 1000 candidates of metal-deficient stars and found a limited but significant fraction of stars with disk orbits ($z_{max} < 3$ kpc and $6 \lesssim r_{max} \lesssim 13$ kpc) and low metallicity ([Fe/H] < -2.5). Our target RRL may belong to the same population. There are a few scenarios to explain the metal-deficient disk population (see, e.g., Sestito et al. 2020). Such a population could compose the ancient disk of the Galaxy present before the severe merger that created the Plume (or the *Gaia-Sausage-Enceladus*) structure around 10 Gyr ago. The formation of the stars contributing to the ancient disk may be *in situ* (within the pre-existent disk) or external. Alternatively, metal-deficient stars with external origins could be quietly merged into the Galactic thick disk even after the severe merger (Gómez et al. 2017; Karademir et al. 2019). If the membership to the thick disk is confirmed, the target

RRL would be a unique object representing the population of the metal-deficient thick disk. Otherwise, the target may be giving a caution for contamination of halo stars to the disk population.

5. CONCLUDING REMARKS

We presented photometric and spectroscopic analysis on an RRL, KISO J 201241.60+321242.4 or HD 331986, located in the Galactic plane at 1 kpc from the Sun. Although this star was found to be an RRL by some previous surveys and is bright ($V \sim 11.3$), no study investigated its detailed characteristics. We confirmed its classification as an RRc-type variable and discovered that it is a very metal-poor star. The near-infrared spectrum taken with the WINERED spectrograph covering 0.9–1.35 µm shows only hydrogen lines but no metallic lines. We estimated the upper limit of metallicity to be [Fe/H] $= -2.5$. This upper limit is consistent with the metallicity inferred from the period–luminosity–metallicity relation, although there remains a large uncertainty, ~ 0.5 dex, in the latter estimate. We conclude that the object is among the known RRLs with the lowest metallicity, around -3.0 to -2.5 dex (Hansen et al. 2011; Crestani et al. 2021a).

This RRL is located within the thick disk and its kinematics is consistent with that of thick-disk objects, which makes it an even more interesting object. While RRLs with [Fe/H] $\gtrsim -1$ tend to have disk-like orbits (Layden 1995; Layden et al. 1996; Prudil et al. 2020; Zinn et al. 2020), metal-deficient RRLs have been regarded as halo objects. Recent studies (e.g., Sestito et al. 2020; Limberg et al. 2021) found the presence of metal-deficient stars (but not RRLs) in the thick disk, which has a large impact on our understanding of the Galactic formation. Finding the origin of the target RRL would give an essential insight into the early history of the Galaxy.

Detailed elemental abundances are crucial for disclosing the origins of stars. However, without any metallic lines detected, we have no clues to the abundance pattern of the target. It is of vital importance to make follow-up spectroscopic observations in the optical range, in which much stronger lines of various elements are present (e.g., Hansen et al. 2011; Crestani et al. 2021b). The origin of our target may be revealed by comparing its abundance pattern with those of RRLs and other stars with similarly low metallicity in different groups including the halo and the thick disk. Furthermore, the census of RRLs in the Galactic plane region has been limited, and future surveys including the *Gaia* observations would reveal more metal-deficient RRLs that are constrained in the disk. A larger sample of such objects and follow-up observations would enable us to understand the initial environment and formation of the ancient Galactic disk.

REFERENCES

Andrievsky, S., Wallerstein, G., Korotin, S., et al. 2018, PASP, 130, 024201

Andrievsky, S. M., Wallerstein, G., Korotin, S. A., et al. 2020, Astronomische Nachrichten, 341, 899

Bailer-Jones, C. A. L., Rybizki, J., Fouesneau, M., et al. 2021, AJ, 161, 147

Beaton, R. L., Bono, G., Braga, V. F., et al. 2018, SSRv, 214, 113

Beers, T. C. & Christlieb, N. 2005, ARA&A, 43, 531

Beers, T. C., Norris, J. E., Placco, V. M., et al. 2014, ApJ, 794, 58

Belokurov, V., Erkal, D., Evans, N. W., et al. 2018, MNRAS, 478, 611

Benkő, J. M., Sódor, Á., & Pál, A. 2021, MNRAS, 500, 2554

Bland-Hawthorn, J. & Gerhard, O. 2016, ARA&A, 54, 529

Bovy, J. 2015, ApJS, 216, 29

Braga, V. F., Crestani, J., Fabrizio, M., et al. 2021, ApJ, 919, 85

Chadid, M., Sneden, C., & Preston, G. W. 2017, ApJ, 835, 187

Chen, X., Wang, S., Deng, L., et al. 2018, ApJS, 237, 28

Chiba, M. & Beers, T. C. 2000, AJ, 119, 2843

Clementini, G., Ripepi, V., Molinaro, R., et al. 2019, A&A, 622, A60

Crestani, J., Braga, V. F., Fabrizio, M., et al. 2021a, ApJ, 914, 10

Crestani, J., Fabrizio, M., Braga, V. F., et al. 2021b, ApJ, 908, 20

Da Costa, G. S., Bessell, M. S., Mackey, A. D., et al. 2019, MNRAS, 489, 5900

Di Matteo, P., Spite, M., Haywood, M., et al. 2020, A&A, 636, A115

Dinescu, D. I. 2002, ASPC, 265, 365

Evans, D. W., Riello, M., De Angeli, F., et al. 2018, A&A, 616, A4

Fabrizio, M., Braga, V. F., Crestani, J., et al. 2021, ApJ, 919, 118

Fernández-Alvar, E., Kordopatis, G., Hill, V., et al. 2021, MNRAS, 508, 1509

Frebel, A. & Norris, J. E. 2015, ARA&A, 53, 631

Gaia Collaboration, Brown, A. G. A., Vallenari, A., et al. 2021, A&A, 649, A1

Gallart, C., Bernard, E. J., Brook, C. B., et al. 2019, Nature Astronomy, 3, 932

Gómez, F. A., Grand, R. J. J., Monachesi, A., et al. 2017, MNRAS, 472, 3722

Govea, J., Gomez, T., Preston, G. W., et al. 2014, ApJ, 782, 59

Gullikson, K., Dodson-Robinson, S., & Kraus, A. 2014, AJ, 148, 53

Hansen, C. J., Nordström, B., Bonifacio, P., et al. 2011, A&A, 527, A65

Helmi, A. 2020, ARA&A, 58, 205

Helmi, A., Babusiaux, C., Koppelman, H. H., et al. 2018, Nature, 563, 85

Helmi, A., White, S. D. M., de Zeeuw, P. T., et al. 1999, Nature, 402, 53

Hoffman, D. I., Harrison, T. E., & McNamara, B. J. 2009, AJ, 138, 466

Ikeda, Y., Kobayashi, N., Kondo, S., et al. 2016, Proc. SPIE, 9908, 99085Z

Ikeda, Y., Kobayashi, N., Kondo, S., et al. 2021, PASP, in press

Iorio, G. & Belokurov, V. 2021, MNRAS, 502, 5686

Jayasinghe, T., Kochanek, C. S., Stanek, K. Z., et al. 2018, MNRAS, 477, 3145

Jofré, P., Heiter, U., & Soubiran, C. 2019, ARA&A, 57, 571

Karademir, G. S., Remus, R.-S., Burkert, A., et al. 2019, MNRAS, 487, 318

Kennedy, C. R., Stancliffe, R. J., Kuehn, C., et al. 2014, ApJ, 787, 6

Kinemuchi, K., Smith, H. A., Woźniak, P. R., et al. 2006, AJ, 132, 1202

Kinman, T. D., Aoki, W., Beers, T. C., et al. 2012, ApJL, 755, L18

Layden, A. C. 1995, AJ, 110, 2288

Layden, A. C., Hanson, R. B., Hawley, S. L., et al. 1996, AJ, 112, 2110

Limberg, G., Santucci, R. M., Rossi, S., et al. 2021, ApJ, 913, 11

Magurno, D., Sneden, C., Bono, G., et al. 2019, ApJ, 881, 104

Maintz, G. 2005, A&A, 442, 381

Mainzer, A., Bauer, J., Cutri, R. M., et al. 2014, ApJ, 792, 30

Mainzer, A., Bauer, J., Grav, T., et al. 2011, ApJ, 731, 53

Matsunaga, N. 2017, European Physical Journal Web of Conferences, 152, 01027

Matteucci, F. 2021, arXiv:2106.13145

Meléndez, J. & Barbuy, B. 1999, ApJS, 124, 527

Mészáros, S., Allende Prieto, C., Edvardsson, B., et al. 2012, AJ, 144, 120

Mullen, J. P., Marengo, M., Martínez-Vázquez, C. E., et al. 2021, ApJ, 912, 144

Neeley, J. R., Marengo, M., Bono, G., et al. 2017, ApJ, 841, 84

Neeley, J. R., Marengo, M., Freedman, W. L., et al. 2019, MNRAS, 490, 4254

Oliva, E., Origlia, L., Scuderi, S., et al. 2015, A&A, 581, A47

Preston, G. W., Thompson, I. B., Sneden, C., et al. 2006, AJ, 132, 1714

Prudil, Z., Dékány, I., Grebel, E. K., et al. 2020, MNRAS, 492, 3408

Ren, F., de Grijs, R., Zhang, H., et al. 2021, AJ, 161, 176

Ryabchikova T., Piskunov N., Kurucz R. L., et al. 2015, Phys. Scr., 90, 054005

Sako, S. et al. 2012, Proc. SPIE, 8446, 6L

Schönrich, R., Binney, J., & Dehnen, W. 2010, MNRAS, 403, 1829

Sestito, F., Martin, N. F., Starkenburg, E., et al. 2020, MNRAS, 497, L7

Skrutskie, M. F., Cutri, R. M., Stiening, R., et al. 2006, AJ, 131, 1163

Sneden, C., Bean, J., Ivans, I., et al. 2012, MOOG: LTE line analysis and spectrum synthesis, Astrophysics Source Code Library (ascl:1202.009)

Sneden, C., Preston, G. W., Chadid, M., et al. 2017, ApJ, 848, 68

Sneden, C., Preston, G. W., Kollmeier, J. A., et al. 2018, AJ, 155, 45

Starkenburg, E., Martin, N., Youakim, K., et al. 2017, MNRAS, 471, 2587

Tody, D. 1986, Proc. SPIE, 733

Tody, D. 1993, Astronomical Data Analysis Software and Systems II, 173

VanderPlas, J. T. 2018, ApJS, 236, 16

Vasiliev, E. 2019, MNRAS, 482, 1525

Wang, S. & Chen, X. 2019, ApJ, 877, 116

Wallerstein, G., Gomez, T., & Huang, W. 2012, Ap&SS, 341, 89

Zinn, R., Chen, X., Layden, A. C., et al. 2020, MNRAS, 492, 2161